



HAL
open science

Transient and steady states of $Gd_2Zr_2O_7$ and $2ZrO_2 \cdot Y_2O_3$ (ss) interactions with calcium magnesium aluminium silicates

Sandrine Nathalie Duluard, Elodie Delon, Jean-Pierre Bonino, André Malié, Aurélien Joulia, Luc Bianchi, Philippe Gomez, Florence Ansart

► To cite this version:

Sandrine Nathalie Duluard, Elodie Delon, Jean-Pierre Bonino, André Malié, Aurélien Joulia, et al.. Transient and steady states of $Gd_2Zr_2O_7$ and $2ZrO_2 \cdot Y_2O_3$ (ss) interactions with calcium magnesium aluminium silicates. *Journal of the European Ceramic Society*, 2019, 39 (4), pp.1451-1462. 10.1016/j.jeurceramsoc.2018.12.016 . hal-02115096

HAL Id: hal-02115096

<https://hal.science/hal-02115096>

Submitted on 30 Apr 2019

HAL is a multi-disciplinary open access archive for the deposit and dissemination of scientific research documents, whether they are published or not. The documents may come from teaching and research institutions in France or abroad, or from public or private research centers.

L'archive ouverte pluridisciplinaire **HAL**, est destinée au dépôt et à la diffusion de documents scientifiques de niveau recherche, publiés ou non, émanant des établissements d'enseignement et de recherche français ou étrangers, des laboratoires publics ou privés.



Open Archive Toulouse Archive Ouverte (OATAO)

OATAO is an open access repository that collects the work of Toulouse researchers and makes it freely available over the web where possible

This is an author's version published in: <http://oatao.univ-toulouse.fr/23787>

Official URL: <https://doi.org/10.1016/j.jeurceramsoc.2018.12.016>

To cite this version:

Duluard, Sandrine Nathalie  and Delon, Elodie  and Bonino, Jean-Pierre  and Malié, André and Joulia, Aurélien and Bianchi, Luc and Gomez, Philippe and Ansart, Florence  *Transient and steady states of Gd₂Zr₂O₇ and 2ZrO₂·Y₂O₃ (ss) interactions with calcium magnesium aluminium silicates.* (2019) *Journal of the European Ceramic Society*, 39 (4). 1451-1462. ISSN 0955-2219

Any correspondence concerning this service should be sent to the repository administrator: tech-oatao@listes-diff.inp-toulouse.fr

Transient and steady states of $Gd_2Zr_2O_7$ and $2ZrO_2 \cdot Y_2O_3$ (ss) interactions with calcium magnesium aluminium silicates

Sandrine Duluard^{a,*}, Elodie Delon^a, Jean-Pierre Bonino^a, André Malie^b, Aurélien Joulia^c,
Luc Bianchi^b, Philippe Gomez^d, Florence Ansart^a

^a CIRIMAT, Université de Toulouse, CNRS, INPT, UPS, Université Toulouse 3 Paul Sabatier, Bât CIRIMAT, 118 Route de Narbonne, 31062 Toulouse cedex 9, France

^b SAFRAN AIRCRAFT ENGINES Site de Châtelleraut, Z.I. Nord, rue Maryse Bastié, BP 129, 86101 Châtelleraut Cedex, France

^c SAFRAN Tech, Pôle Matériaux et Procédés, rue des Jeunes Bois, Châteaufort, CS 80112, 78772 Magny-Les-Hameaux, France

^d DGA Techniques aéronautiques, 47 rue Saint Jean – 93123, 31131 Balma, France

ARTICLE INFO

Keywords:

$Gd_2Zr_2O_7$

$2ZrO_2 \cdot Y_2O_3$ (ss)

Reaction products

Kinetics

CMAS tightness

ABSTRACT

Reactions between calcium magnesium aluminium silicates (CMAS) and $Gd_2Zr_2O_7$ or $2ZrO_2 \cdot Y_2O_3$ (ss) are investigated within a temperature range of 1200–1300 °C and for durations of 1 h–100 h. The evolution of CMAS penetration depth in $Gd_2Zr_2O_7$ and $2ZrO_2 \cdot Y_2O_3$ (ss) pellets varies considerably depending on the interaction time. A quantitative analysis of the nature and composition of phases observed in stationary conditions (powder/powder interaction) is performed by SEM-FEG coupled with WDS analyses using micro-agglomerated nanoparticles of $Gd_2Zr_2O_7$ and $2ZrO_2 \cdot Y_2O_3$. Faster kinetics of the gadolinium-based system are illustrated through an analysis of the morphology of the reaction area and of the resulting CMAS tightness of reaction products. The compositions and quantities of reaction products observed at equilibrium are very similar for the two systems, but transient states are significantly different.

1. Introduction

With improvements made to metal parts and thermal barrier coatings (TBCs), aero-engine working temperatures have increased in addition to their efficiency [1,2]. However, as a result, TBCs are subjected to a new form of degradation: corrosion at high temperatures by molten calcium-magnesium-alumino-silicates (CMASs) [3,4]. These compounds are naturally found on Earth (e.g., in volcanic ash, sand, dust or even pollution) [5], and their silicon ratios vary in addition to levels of elements such as iron, nickel, vanadium, etc. [6–9]. As operating temperatures exceed the glass transition or even the melting temperature of most CMAS compounds, CMAS interactions with TBCs are detected. Due to their high wettability and low viscosity [10], molten CMAS infiltrates the porosity/cracks of the TBC, resulting in severe levels of thermochemical and thermomechanical degradation [11,12]. The molten CMAS then infiltrates the TBC, leading to the degradation of the morphology of TBCs [4,10,12]. Moreover, the dissolution of 8YSZ TBCs in molten CMAS generally leads to the precipitation of undesired monoclinic zirconia through the leaching of yttrium from metastable tetragonal zirconia t' solid solutions and in parallel through the formation of silicide-type reaction products [13]. Moreover, with cooling, molten CMAS becomes solid while TBC becomes rigid and loses its

strain tolerance [5,12]. CMAS corrosion leads to TBC delamination, obstruction of cooling channels, etc. [14–16].

These issues have led motorists to revise the specifications of turbine blade coatings and to develop systems more resistant to CMAS corrosion at high temperatures [13]. Several authors have demonstrated an interest in oxides of yttrium Y, gadolinium Gd and other rare earths RE^{3+} (RE: La, Nd, Ce, Er, Eb, and Yb) in the form of simple oxides or of pyrochlore-based oxides $A_2B_2O_7$ [13,17–21]. Indeed, rare earth zirconates present thermal conductivity similar to that of YSZ: $1.6 \text{ W} \cdot \text{m}^{-1} \cdot \text{K}^{-1}$ for $Gd_2Zr_2O_7$ [22] and $1.8 \text{ W} \cdot \text{m}^{-1} \cdot \text{K}^{-1}$ for $2ZrO_2 \cdot Y_2O_3$ at 700 °C [23] versus roughly $1.7 \text{ W} \cdot \text{m}^{-1} \cdot \text{K}^{-1}$ for YSZ. Such materials have been explored as alternative TBCs or as protective coatings for existing TBCs [25]. For protective coatings, a low coefficients of thermal expansion (CTE) mismatch is required between the rare earth zirconates and YSZ TBCs. This is the case with $11.6 \cdot 10^{-6} \text{ K}^{-1}$ and $9.15 \cdot 10^{-6} \text{ K}^{-1}$ CTEs for $Gd_2Zr_2O_7$ and $2ZrO_2 \cdot Y_2O_3$ (ss), respectively, while for YSZ, it is equal to $11 \cdot 10^{-6} \text{ K}^{-1}$ [22,24]. Related requirements are numerous. An anti-CMAS coating presents strong reaction kinetics with molten CMAS. Reaction products must be solid and stable at high temperatures, and they must seal the porosity, voids or cracks of a thermal barrier coating to limit the infiltration of CMAS during a future attack. Eventually, the anti-CMAS coating must trap a large volume of

* Corresponding author at: CIRIMAT, Université Toulouse 3 Paul Sabatier, 118 Route de Narbonne, 31062 Toulouse cedex 9, France.

E-mail address: duluard@chimie.ups-tlse.fr (S. Duluard).

CMAS elements (Ca^{2+} , Mg^{2+} , Al^{3+} , and Si^{4+}) while the CMAS tightness of the reaction product layer is a central requirement [21,26–30].

Poerschke [31] observed the calcia-silica-yttria system at 1400 °C and 1600 °C. He identified the formation of different phases: Ca/Y-cyclosilicate $\text{Ca}_3\text{Y}_2\text{Si}_6\text{O}_{26}$, silico-carnotite $\text{Ca}_3\text{Y}_2\text{Si}_3\text{O}_{12}$, cuspidine $\text{Ca}_2\text{Y}_2\text{Si}_2\text{O}_9$ and apatite solid solution based on $\text{Ca}_2\text{Y}_8\text{Si}_6\text{O}_{26}$. Theoretically, the apatite phase occurs between $\text{Ca}_4\text{Y}_6(\text{SiO}_4)_6(\text{O})$ and $\text{Y}_{9.33}\text{Si}_{10.67}(\text{SiO}_4)_6\text{O}_2$, and his study reveals the extent of the solid solution homogeneity range for the apatite phase of $\text{Ca}_{0.5}\text{Y}_{0.5}\text{Si}_9(\text{SiO}_4)_6\text{O}_2$ and $\text{Ca}_{2.5}\text{Y}_7.5(\text{SiO}_4)_6\text{O}_{1.75}$. In another paper, Poerschke [26] compares the influence of the composition of deposited thermal barrier oxides (TBOs). Indeed, the reaction of TBOs and molten CMAS depends on several criteria: the composition of the molten CMAS, the ratio $\text{ZrO}_2:\text{REO}_{1.5}$ in the TBO and the nature of $\text{REO}_{1.5}$. Main reaction products involved are apatite and zircon phases. For $\text{YO}_{1.5}$ -TBO, crystalline silicates including yttrium disilicate, garnet and silicocarnotite form.

In reference to gadolinium zirconate $\text{Gd}_2\text{Zr}_2\text{O}_7$, Wang [32,33] observed interactions occurring between molten CMAS and $\text{Gd}_2\text{Zr}_2\text{O}_7$ at 1300 °C for 5 h. The main reaction products are apatite phase $\text{Ca}_2\text{Gd}_8(\text{SiO}_4)_6\text{O}_2$ and a zirconium-enriched cubic fluorite phase depleted in gadolinium $\text{Zr}_2\text{Gd}_{2-x}\text{O}_7$. These results are confirmed by the work of Poerschke on ternary diagram $\text{CaO}-\text{Gd}_2\text{O}_3-\text{SiO}_2$ observed at 1400 °C and 1600 °C [34]. Stable phases observed at 1400 °C are silicocarnotite $\text{Ca}_3\text{Gd}_2\text{Si}_3\text{O}_{12}$, cyclosilicate $\text{Ca}_3\text{Gd}_2\text{Si}_6\text{O}_{26}$ and apatite solid solution, for which compositions extend from $\text{Gd}_{9.33}(\text{SiO}_4)_6\text{O}_2$ to $\text{Ca}_{2.75}\text{Gd}_{7.25}(\text{SiO}_4)_6\text{O}_{1.625}$. At 1600 °C, the liquid coexists with crystalline phase SiO_2 , apatite and $\text{Ca}_2\text{Gd}_2\text{Si}_2\text{O}_9$. The wide range of liquid stable compositions found in contact with apatite phase shows that this phase is predominant in crystallization products formed for reactions occurring between $\text{GdO}_{1.5}$ -based TBC and oxides CaO and SiO_2 . In another study Kramer [35] examined infiltration by molten CMAS of $\text{Gd}_2\text{Zr}_2\text{O}_7$ -based TBC synthesized by EB-PVD. According to his results, main reaction products are $\text{Ca}_2\text{Gd}_8(\text{SiO}_4)_6\text{O}_2$ -based apatite and Zr, Gd rich fluorite phases with small volumes of calcium. He proved that these products fill the columnar porosity of EB-PVD TBC and prevent the infiltration of molten CMAS. Finally, these analyses show that the formed apatite is substituted with zirconium according to the following formula: $\text{Gd}_{6-y}\text{Zr}_y[\text{Gd}_{2-2z+y}/3\text{Ca}_{2+z}](\text{SiO}_4)_6\text{O}_2$.

Drexler [36,37] studied interactions occurring between CMAS/ $\text{Gd}_2\text{Zr}_2\text{O}_7$ and CMAS/ $2\text{ZrO}_2\text{Y}_2\text{O}_3$ (ss) with a CMAS composition 39.2 mol% CaO – 5.2 mol% MgO – 4.1 mol% $\text{AlO}_{1.5}$ – 51.5 mol% SiO_2 , i.e., abbreviated formula $\text{C}_{39.2}\text{A}_{4.1}\text{M}_{5.2}\text{S}_{51.5}$. Apatite phase and cubic fluorite phase enriched in zirconium formed. In studying infiltration at 1200 °C over 24 h of CMAS for pellets of 15% porosity, he demonstrated that CMAS penetration depths reach 20 μm and 60 μm for the $2\text{ZrO}_2\text{Y}_2\text{O}_3$ (ss) system and $\text{Gd}_2\text{Zr}_2\text{O}_7$, respectively. His interpretation is that molten CMAS must penetrate deeper into a $\text{Gd}_2\text{Zr}_2\text{O}_7$ pellet to accumulate enough Gd^{3+} cations to form the Gd-apatite phase. By extension, he concludes that TBC composed of $\text{RE}_2\text{Zr}_2\text{O}_7$ with rare earth cations larger than those of Gd^{3+} cations but similar to those of Ca^{2+} cations (e.g., Sm^{3+} , Nd^{3+} , Ce^{3+} , and La^{3+}) may not be sufficiently effective, as they form an RE rich apatite phase $(\text{Ca}_2\text{RE}_2)\text{RE}_6(\text{SiO}_4)_6\text{O}_2$ type [13,17,32,33,35,38–42]. Conversely, Drexler focused on $\text{RE}_2\text{Zr}_2\text{O}_7$ TBC with a RE^{3+} size of less than Y^{3+} . For example, $\text{Yb}_2\text{Zr}_2\text{O}_7$ reactions with molten CMAS result in the formation of apatite phase $\text{Ca}_2\text{Yb}_6(\text{SiO}_4)_6\text{O}_2$ and fluorite phase enriched with zirconium and with little ytterbium. However, the penetration depth of CMAS is high (40 μm) due to kinetics of the crystallization of RE-apatite, which tend to decline with RE^{3+} size [43]. Finally, $\text{RE}_2\text{Zr}_2\text{O}_7$ -based TBC, for which rare earth RE^{3+} cations present a lower ionic radius than yttrium Y^{3+} cations (e.g., Er^{3+} , Yb^{3+} , and Lu^{3+}), are less effective than $2\text{ZrO}_2\text{Y}_2\text{O}_3$ (ss) and even when these systems form $\text{Ca}_4\text{RE}_6(\text{SiO}_4)_6\text{O}_2$. Drexler focused on interactions observed at 1200 °C for a $\text{C}_{39.2}\text{A}_{4.1}\text{M}_{5.2}\text{S}_{51.5}$ composition with a higher viscosity than that of $\text{C}_{33}\text{M}_9\text{A}_{13}\text{S}_{45}$ [44]. Krause [45] conducted model experiments on hollow spheres of

$2\text{ZrO}_2\text{Y}_2\text{O}_3$ (ss) and concluded that high concentrations of Y^{3+} in a confined volume are required for the formation of the apatite phase.

In this paper, the temperature dependence of $\text{Gd}_2\text{Zr}_2\text{O}_7$ and $2\text{ZrO}_2\text{Y}_2\text{O}_3$ performance is explored over an extended temperature and time range: 1200 °C for normal operating conditions and 1250 °C and 1300 °C for peak temperatures (take-off and landing) over 1 h to 100 h. The Ca-Mg-Al silicate composition used in this study is as follows: 33.2 wt% CaO – 6.5 wt% MgO – 11.9 wt% Al_2O_3 – 45 wt% SiO_2 , i.e., a molar composition of 33 mol% CaO – 9 mol% MgO – 13 mol% $\text{AlO}_{1.5}$ – 48.5 mol% SiO_2 abbreviated in the following as $\text{C}_{33}\text{M}_9\text{A}_{13}\text{S}_{45}$. These conditions are representative of the average chemical composition of CMAS found in some real parts [5] and have been frequently used in the literature [10,11,46–48]. The melting temperature reported for this CMAS composition is 1233 °C, and its calculated glass transition temperature is 764 °C [44]. The study first focuses on pellets (2D interaction) to determine the thickness of the reaction layer as function of the reaction duration. Then, a 3D configuration (powder/powder interaction) of a 30/70 anti-CMAS / CMAS ratio is studied to understand reaction products, volumes and morphologies. Conditions applied are more stationary than those of pellet infiltration. The anti-CMAS raw material powder consists of spherical agglomerates. Reaction product compositions and information on the kinetics of reactions are extracted from SEM FEG observations and WDS analyses. The objective of the study is to address two issues related to CMAS mitigation: the importance of the composition of the reaction products relative to the kinetics of their formation and differences observed between system transient and steady states.

2. Materials and methods

2.1. CMAS composition and preparation

The CMAS $\text{C}_{33}\text{M}_9\text{A}_{13}\text{S}_{45}$ was prepared from single oxides of calcium (CaO , Aldrich, purity $\geq 99\%$), magnesium (MgO , Sigma-Aldrich, purity $\geq 99\%$), aluminium (Al_2O_3 , Sigma-Aldrich, purity $\geq 99\%$) and silicon (SiO_2 , Aldrich, purity $\geq 99.9\%$). The compounds were mixed with ultra-pure water and dried at roughly 80 °C for 12 h. They were then placed in a platinum crucible and heated at 1400 °C for one hour. After quenching with water, the glassy material was manually ground to obtain CMAS powder. The melting temperature determined by TG-DTA was set to 1230 ± 5 °C, which is comparable to the value given in the literature (1233 °C [44]).

2.2. Anti-CMAS powders

As anti-CMAS powders we used commercial $\text{Gd}_2\text{Zr}_2\text{O}_7$ and $2\text{ZrO}_2\text{Y}_2\text{O}_3$ (ss) from Treibacher with purity levels exceeding 99%. They are composed of submicronic particles agglomerated in several micron spheres (cf Fig. 1).

2.3. Pellet preparation

Dense pellets (densities of > 90–95% on pellet surfaces) were prepared by Spark Plasma Sintering (SPS) from each anti-CMAS powder. The powders were pressed in a uniaxial press. No binder was used. The pressed powder was subjected to Joule heating in an SPS system. Pellets were annealed at 1500 °C over 5 min under a pressure level of 31.4 kN in a 25 mm diameter graphite mould. A graphite paper was placed between the powder and the mould. Pressure was applied throughout the temperature plateau. The paper was removed by post-thermal treatment applied at 900 °C over 10 h under air.

2.4. Interaction test procedures

CMAS powder / anti-CMAS pellet interactions were analysed by depositing CMAS powder onto the surfaces of the anti-CMAS pellets at a

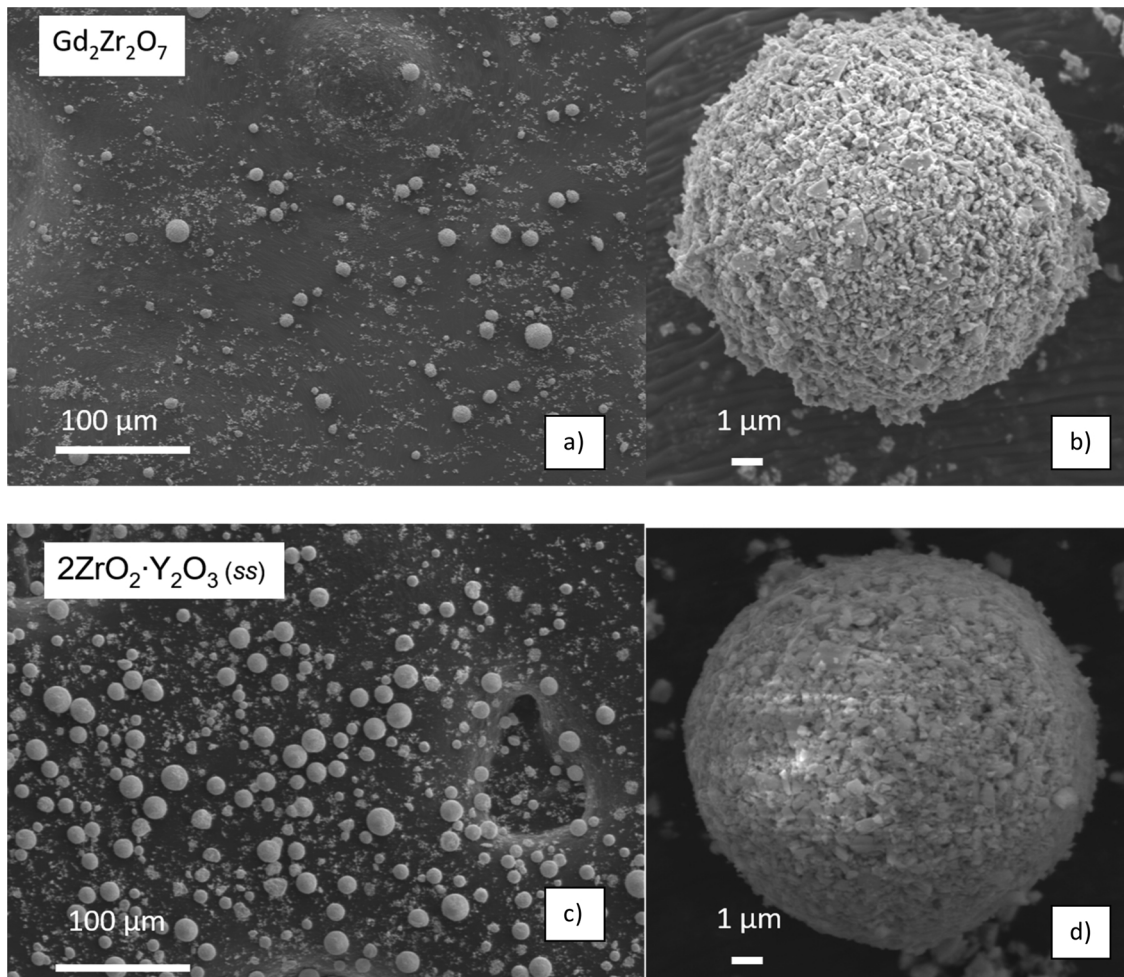


Fig. 1. Scanning electron microscopy of the as-received Gd₂Zr₂O₇ powder (a) and b) as-received 2ZrO₂·Y₂O₃ (ss) powder (c) and d).

contamination rate of 10 mg/cm². This rate corresponds to typical contamination rates given in the literature [13,36].

For the CMAS powder / anti-CMAS powder interactions, the equimass mixing of an anti-CMAS powder with CMAS was performed for cations with a molar ratio of 0.7 C₃₃M₉A₁₃S₄₅ / 0.3 RE₅₀Zr₅₀ (RE₂Zr₂O₇). The two powders were manually mixed in a mortar. The anti-CMAS agglomerates were not fully broken through this technique. The mixed powders were placed in a platinum crucible in a preheated furnace. After heating, the cooling rate was determined by the furnace inertia (cooling rate of approx. 50 °C/h).

2.5. Characterizations

X-ray diffraction analyses were conducted using an automated Bruker D4 Endeavor diffractogram of the Θ -2 Θ configuration. An anticathode of copper (λ (CuK _{α 1}) = 0.15406 nm, λ (CuK _{α 2}) = 0.15444 nm) generated X-rays. Analyses were carried out within an angular range of 10° to 100° with a measurement step of 0.016° and with a counting time of 0.15 s per step. Phase identification was applied using EVA software databases.

Anti-CMAS powders were characterized by Raman spectroscopy with a Raman Horiba Jobin Yvon Labram HR 800 spectrometer equipped with a confocal microscope and a 532 nm laser.

The identification of the apatite phase is not possible via XRD, as cell parameters of Ca₄Y₆(SiO₄)₆O and Ca₂Y₈(SiO₄)₆O₂ are very similar (a = 9.356 Å and c = 6.793 Å (JPCDS file: 00-027-0093) for Ca₄Y₆-apatite while for Ca₂Y₈-apatite, a = 9.36 Å and c = 6.78 Å (JPCDS file: 04-006-0319)). Then were analysed by Electron Probe Microanalysis

(EPMA). For EPMA, the field emission Cameca SXFive FE microprobe was used with an acceleration voltage of 10 keV and a probe current of 30 nA. Under these conditions, the minimum observable feature was smaller than one micron. Chemical compositions were calculated from the PAP (Pouchou and Pichoir [49]) correction model. As standard specimens we used periclase MgO (K α -ray) for Mg; gadolinium orthophosphate GdPO₄ (L α -ray) for Gd; wollastonite CaSiO₃ (K α -ray) for Ca and Si; yttrium orthophosphate YPO₄ (L α -ray) for Y; corundum Al₂O₃ (K α -ray) for Al; and zircon SiZrO₄ (L α -ray) for Zr. Oxygen content levels were calculated from the theoretical stoichiometry of the compounds. EPMA was used to measure the composition of each phase and of the residual CMAS. A 0.1% accuracy level was classically considered for EPMA versus 1% for the EDS analyses. For reaction product compositions, analyses were conducted of the central regions of the grains. For residual CMAS compositions, local measurements were made at a controlled distance of 10 μm from reaction product grains. The results presented in this paper correspond to an average value of over roughly 30 points for each phase. Oxygen content levels were deduced from cation content.

We employed the JEOL JSM-7800 F Prime as a field-emission gun scanning electronic microscopy SEM-FEG microscope for sample characterization. Observations were made in both secondary and back-scattered electron modes. Volumes of reaction products formed during CMAS attacks were determined by image analysis using ImageJ software.

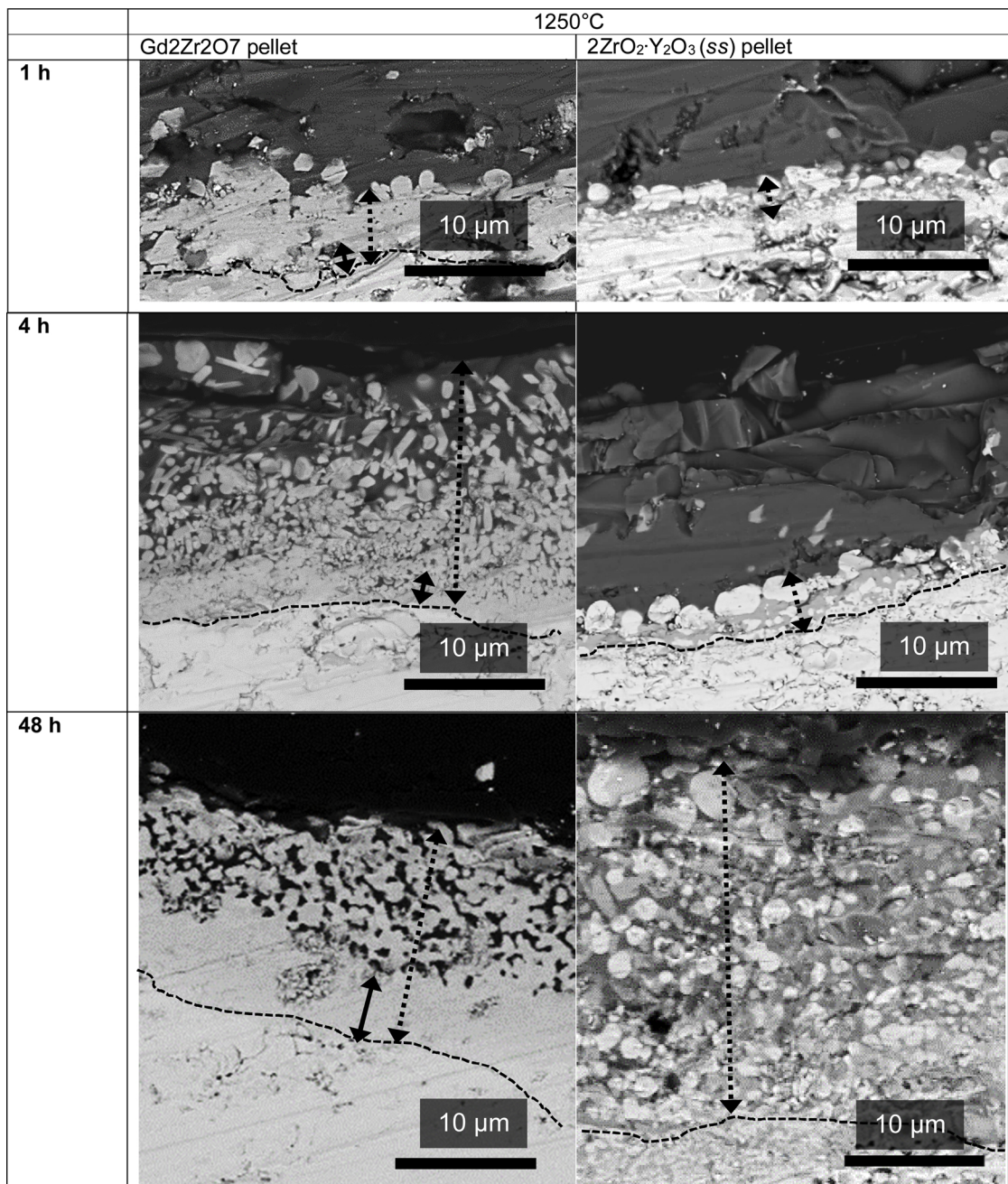


Fig. 2. SEM images of a cross-section of pellet / CMAS interaction zones observed after annealing at 1250 °C for 1 h, 4 h and 48 h for anti-CMAS Gd₂Zr₂O₇ and 2ZrO₂·Y₂O₃ (ss) pellets contaminated with 10 mg CMAS per cm². Dashed lines mark the interface between reaction products and the non-reacted pellet. Dashed arrows denote the reaction product thickness while solid arrows highlight the continuous reaction product layer.

3. Results

3.1. D interactions of CMAS between Gd₂Zr₂O₇ and 2ZrO₂·Y₂O₃ (ss): CMAS on anti-CMAS pellets

The objective of this study was to evaluate the behaviours of different anti-CMAS systems towards a CMAS reaction front. Dense pellets were subjected to CMAS attack at 1200 °C for 48 h; at 1250 °C for 1 h, 4 h and 48 h and at 1300 °C for 4 h and 48 h. Microscopic images of interaction zones observed after 1 h, 4 h, and 48 h hours of interaction at 1250 °C are presented in Fig. 2.

Very dense pellets were used to curtail effects of pellet morphologies on infiltration kinetics and to thus study anti-CMAS effects independently. Thus, in this study the thickness of reaction products only

depends on reaction kinetics and on the permeability of reaction products [26]. Either the system is not CMAS tight and reaction products form continuously or for an efficient anti-CMAS system the reaction product layer is CMAS tight and infiltration is stopped.

The evolution of the morphologies of reaction products of Gd₂Zr₂O₇ and 2ZrO₂·Y₂O₃ (ss) systems annealed at 1250 °C for 1 h, 4 h and 48 h varies. For the Gd₂Zr₂O₇ system, a continuous front of reaction products appears at the interface between the unreacted pellet and the CMAS front. The reaction front includes two parts: a continuous layer that is biphasic (composed of fluorite and apatite as demonstrated below) and a part with reaction products dispersed across the remaining CMAS. For 2ZrO₂·Y₂O₃ (ss) a loose mixture of reaction products is observed across the interaction zone. The reaction product front of 2ZrO₂·Y₂O₃ (ss) and CMAS reactions includes a mixture of reaction products and CMAS

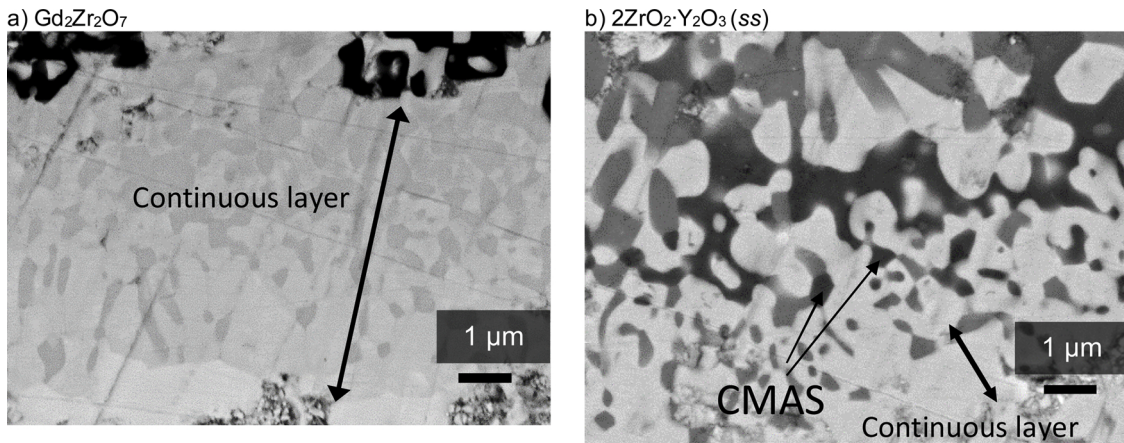


Fig. 3. SEM images of the interface between non-reacted anti-CMAS pellets and reaction products for a) $Gd_2Zr_2O_7$ and b) $2ZrO_2 \cdot Y_2O_3(ss)$ after 48 h of interaction at $1300^\circ C$.

while a continuous interface is not present. In this case, several contrasting compositions are observed, showing the presence of phases other than fluorite and apatite as confirmed in the following sections.

Analyses conducted at higher temperatures confirm this tendency with $10 \mu m$ -thick continuous fronts found for $Gd_2Zr_2O_7$ products and with no continuous front found for $2ZrO_2 \cdot Y_2O_3(ss)$ except for a very thin front observed after treatment at $1300^\circ C$ for 48 h (see Fig. 3). However, even in this case the total thickness of reaction products with $2ZrO_2 \cdot Y_2O_3(ss)$ is doubled relative to $Gd_2Zr_2O_7$ such that the thin layer does not efficiently limit further CMAS infiltration (cf. Fig. 3b). This shows however that the reaction product layer morphology can become CMAS tight at higher temperatures as reaction kinetics are enhanced.

For $Gd_2Zr_2O_7$ /CMAS pellets further analyses of the continuous layers (Fig. 4) show that they are more than $2 \mu m$ thick even after only 1 h of interaction at $1250^\circ C$. By contrast, for $2ZrO_2 \cdot Y_2O_3(ss)$, the thickness of the continuous layer is null even after 48 h of sintering at $1200^\circ C$ and $1250^\circ C$.

An analysis of evolution with time on the thickness of reaction products was performed (Fig. 5). At $1250^\circ C$ a constant increase in reaction product thickness with time is observed for $2ZrO_2 \cdot Y_2O_3(ss)$ to reach $40 \mu m$ after 48 h. For $Gd_2Zr_2O_7$, after a slight increase within 4 h, reaction product thicknesses quickly stabilize at values half those of $2ZrO_2 \cdot Y_2O_3(ss)$. As observed by SEM (Fig. 2 for 4 h at $1250^\circ C$), CMAS is still found on pellet surfaces after several hours of interaction at $1250^\circ C$. CMAS is still found on the pellets while stabilization occurs, showing that $Gd_2Zr_2O_7$ limit the further infiltration of CMAS. At $1300^\circ C$ the stability of product thickness over 4 h–48 h is not significant, as it is only a sign of the end of the reaction occurring due to a lack of CMAS present.

Moreover, for the shortest periods, the reaction product layer of $2ZrO_2 \cdot Y_2O_3(ss)$ is thinner than that of $Gd_2Zr_2O_7$. As described above,

$2ZrO_2 \cdot Y_2O_3(ss)$ reaction products are not CMAS tight, and thus the fewer reaction products observed can only be attributed to slow kinetics of product formation (and not to a blocking of CMAS infiltration). With the microstructure of the $2ZrO_2 \cdot Y_2O_3(ss)$ and $Gd_2Zr_2O_7$ pellets being similar, this feature highlights the fast kinetics of $Gd_2Zr_2O_7$ product formation.

This work illustrates different behaviours of the two selected compositions in terms of morphologies of interaction zones, giving rise to more CMAS tight behaviour for $Gd_2Zr_2O_7$ relative to that of $2ZrO_2 \cdot Y_2O_3(ss)$. However, a quantitative analysis is difficult to conduct in such a dynamic configuration. Thus, to quantitatively study properties of the system, a 3D isotropic configuration was applied in the next part of the study as follows. The nature and composition of phases observed as a function of interaction time are examined.

3.2. D interactions between CMAS and Gd and Y zirconate powders

3.2.1. Interaction reaction mechanisms

XRD and Raman analyses were performed to analyse the raw materials and reaction products (Fig. 6). According to these structural analyses and to the literature, $Gd_2Zr_2O_7$ raw material is composed of a mixture of pyrochlore and disordered fluorite phases. $2ZrO_2 \cdot Y_2O_3(ss)$ is a disordered fluorite phase". These results are confirmed by several works [32,50–55].

After 1 h of interaction at $1250^\circ C$, the XRD signal relative to the pyrochlore raw material is not detectable by XRD. The signal of apatite is clearly detected for reaction products of $Gd_2Zr_2O_7$ in parallel with a transition from pyrochlore phases to disordered fluorite. Under these conditions, the main reaction is as follows:

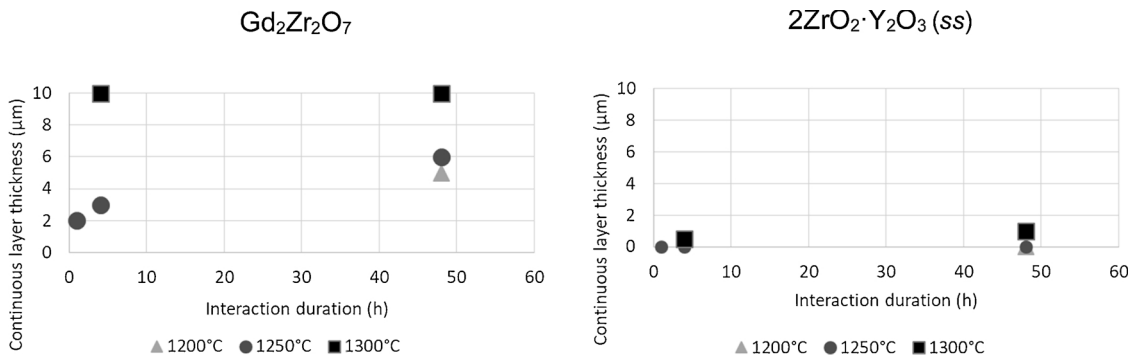
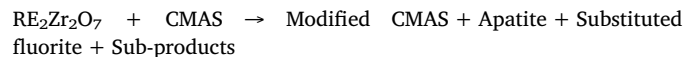


Fig. 4. Continuous reaction product layer thickness as a function of sintering durations and temperatures for $Gd_2Zr_2O_7$ and $2ZrO_2 \cdot Y_2O_3(ss)$ pellets.

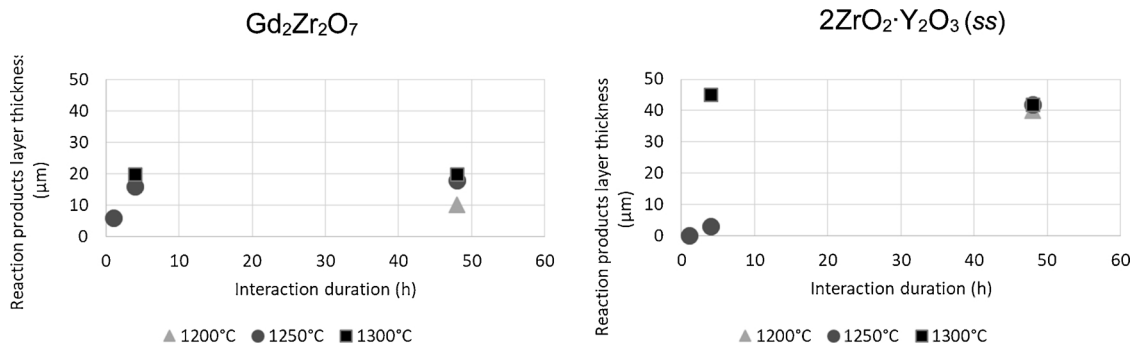


Fig. 5. Reaction product layer thickness depending on the temperature and duration of interactions occurring between $Gd_2Zr_2O_7$ and $2ZrO_2 \cdot Y_2O_3(ss)$ anti-CMAS pellets.

Substitution ions are mainly composed of Gd^{3+} or Y^{3+} cations, but other substitutions in the apatite or fluorite phases are not excluded. The exact compositions of the phases are detailed in paragraph 3.2.2 based on microscopic chemical composition analyses. For $2ZrO_2 \cdot Y_2O_3(ss)$, the signal of apatite is detectable and a slight shift occurs in fluorite signals towards higher angles. The main reaction that occurs is the same as that of $Gd_2Zr_2O_7$. However, a side reaction with the formation of transition garnet phases observed in some of the heat treatment conditions is highlighted in the following sections.

3.2.2. Interaction products: features and proportions

Morphologies and chemical compositions of the reaction products were evaluated from coupling scanning electron microscopic and FEG WDS analyses (accuracy of 0.1 mol%). The microscopic analyses (Fig. 7) reveal the occurrence of faster reactions for $Gd_2Zr_2O_7$ than for $2ZrO_2 \cdot Y_2O_3(ss)$ with two features: the morphology of the interaction zone and the nature of the reaction products. Concerning morphologies of the interaction zone, for the first hours of interaction, reaction products are concentrated in large spherical agglomerates in the case of

$Gd_2Zr_2O_7$ while they are spread across the whole volume of the remaining CMAS for $2ZrO_2 \cdot Y_2O_3(ss)$. With interaction time, Gd-apatite and Gd-fluorite agglomerates disperse within silicate-based glass and an Ostwald-type ripening mechanism is observed in the two systems over long interaction periods.

This can be correlated with the faster kinetics of CMAS reactions occurring with $Gd_2Zr_2O_7$ as discussed in paragraph 4.1.

Phases occurring depending on the anti-CMAS involved are illustrated in Table 1. At equilibrium (100 h of interaction) only fluorite and apatite are present in both $2ZrO_2 \cdot Y_2O_3(ss)$ and Gd zirconate reaction products. This analysis is consistent with the literature on Gd zirconates [26]. In transient states (< 48 h) at 1250 °C and 1300 °C, fluorite and apatite form in both cases after only 1 h of interaction while other phases are found for $2ZrO_2 \cdot Y_2O_3(ss)$. A rough quantitative image analysis shows that 20–25% of the volume is occupied by fluorite while 20% is composed of apatite for $Gd_2Zr_2O_7$ without significant variations occurring with time. For $2ZrO_2 \cdot Y_2O_3(ss)$ the ratios are slightly different with 15% fluorite and 25% apatite found at 1250 °C and with 15–20% fluorite and 25–30% apatite found at 1300 °C. The proportion of garnet

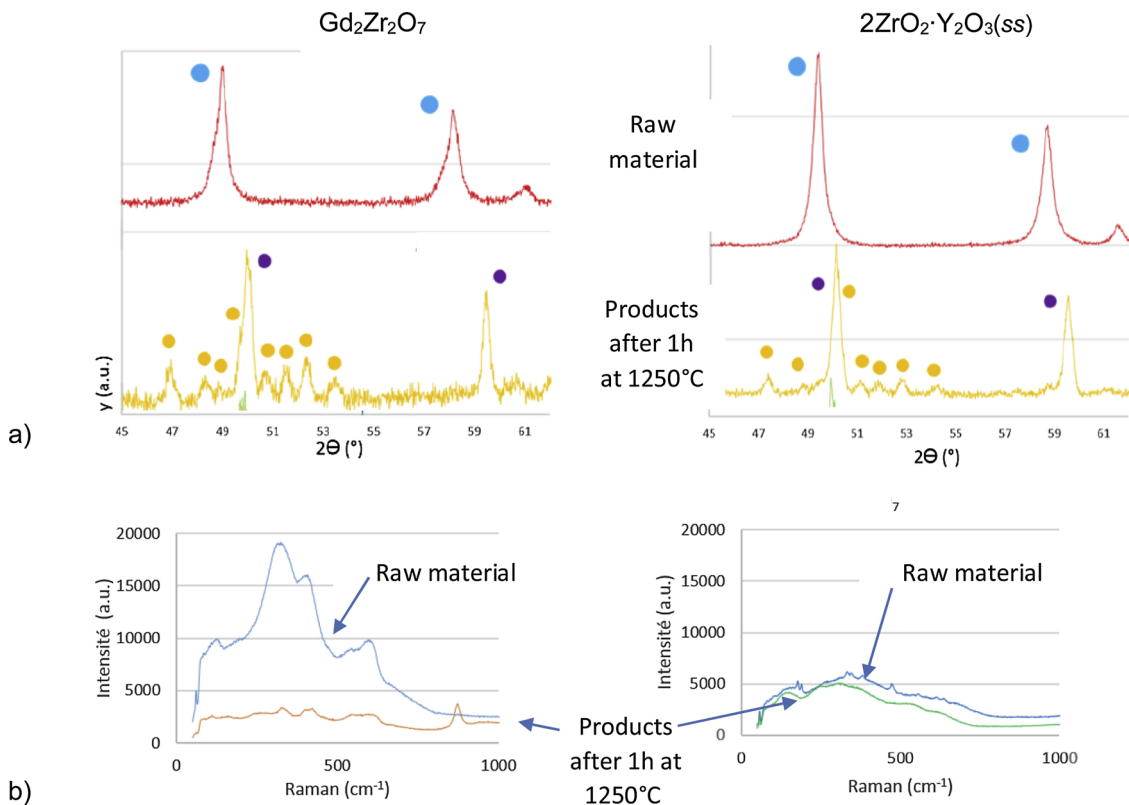


Fig. 6. Structural analyses of raw materials and reaction products derived after 1 h of interaction at 1250 °C: a) XRD and b) Raman spectroscopy.

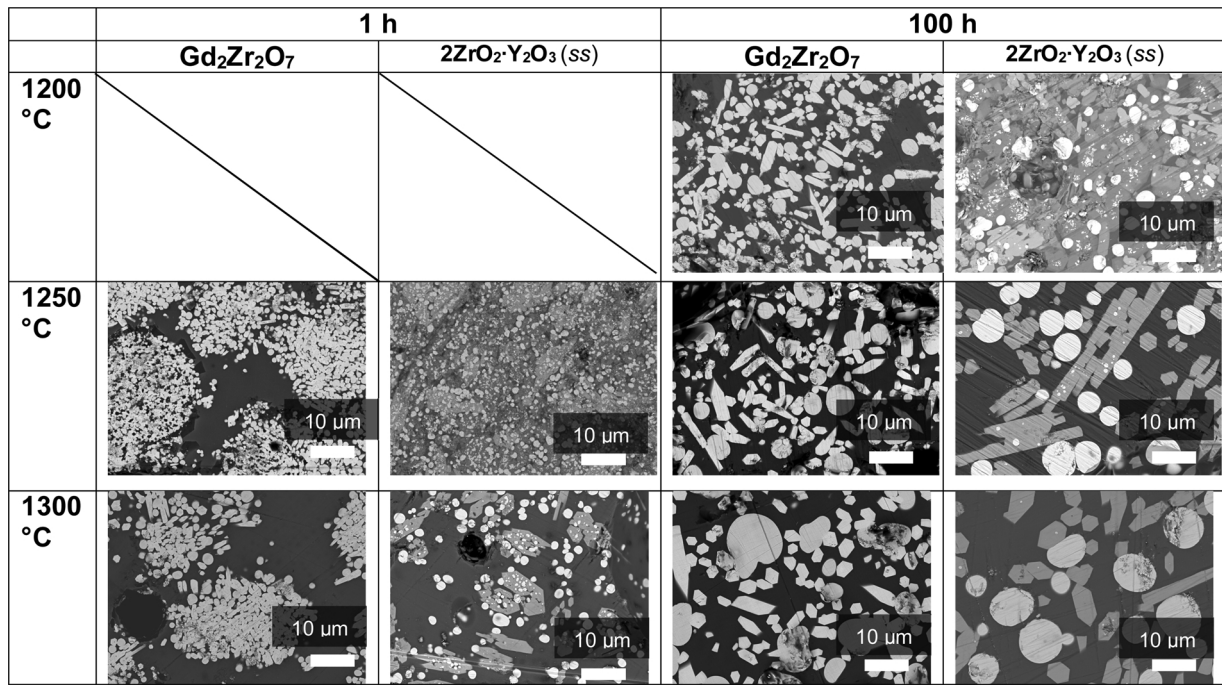


Fig. 7. SEM images of interactions zones observed after reactions between CMAS and anti-CMAS powders and between Gd₂Zr₂O₇ and 2ZrO₂·Y₂O₃ (ss) after 1 h and 100 h of interaction at 1200 °C, 1250 °C and 1300 °C.

phase (phase present in the first stage of interaction at 1250 °C) decreases with annealing time with roughly 10–15% of garnet phase observed after 1 h of interaction, with 7% observed after 48 h and with no garnet phase observed after 100 h. After 100 h at 1300 °C, roughly 60% of the glass remains.

At 1200 °C a major difference is observed between the two anti-CMAS materials: fluorite and apatite form after 24 h of interaction for Gd₂Zr₂O₇ while for 2ZrO₂·Y₂O₃ (ss) only transition phases (garnet and a non-identified phase) are found over this interaction period. Moreover, while for 2ZrO₂·Y₂O₃ (ss) the garnet phase is still present after 48 interactions at 1250 °C, this transition phase is not present after 1 h for Gd₂Zr₂O₇, and only a small proportion (< 2%v) of non-identified phase is observed after less than 24 h of interaction time. This shows that the transition state is shorter for gadolinium zirconate and that the system forms thermodynamically predicted phases (cf thermodynamic data in Poerschke works [26]) from 1250 °C over 1 h. Kinetics are slower for 2ZrO₂·Y₂O₃ (ss); it is necessary to wait a long period at 1250 °C or to heat at higher temperatures (1300 °C) to remove metastable phases

such as garnet phase.

3.2.3. Composition of the apatite phases

Gadolinium and yttrium facilitate a wide range of possible associations to form differently substituted apatite phases. Compositions of apatite observed over different interaction periods and at different temperatures were measured by EPMA and are reported in Table 2.

The results were fit to a generic formula for apatite RE_{6-ya}Zr_{ya}[RE_{2-(2za+ya)/3}Ca_{2+za}](SiO₄)₆O_{xa}. Values of x, y and z as a function of time and temperature are plotted in Fig. 8.

At a given temperature apatite formed from 2ZrO₂·Y₂O₃ (ss) maintains the same composition with time. The most important factor involved is the interaction temperature: Ca and Zr content levels (za and ya, respectively) in apatite increase with increasing temperature. This increase in additional elements of apatite is accompanied by structural defects with the presence of oxygen vacancies (xa decreases). The tendency is the same for Gd₂Zr₂O₇ with only slight changes in za and ya observed with interaction time.

Table 1

Features of the reaction products of CMAS with Gd₂Zr₂O₇ and 2ZrO₂·Y₂O₃ (ss) for the studied interaction temperatures and durations based on WDS and SEM-FEG analyses of a cross-section of equimassic mixtures of CMAS and anti-CMAS.

| Annealing temperature | Annealing time (h) | Gd ₂ Zr ₂ O ₇ | 2ZrO ₂ ·Y ₂ O ₃ (ss) |
|-----------------------|---------------------|--|---|
| 1200 °C | 24 | Liqs + F + Ap + non ident. | Liqs + Gar + non ident. |
| | 48 | Liqs + F + Ap + non ident. | Liqs + Gar + non ident. |
| | 100 | Liqs + F + Ap + non ident. | Liqs + F + Ap + Gar |
| 1250 °C | 1 | Liqs + F + Ap (+ non ident.) | Liqs + F + Ap + Gar |
| | 4 | Liqs + F + Ap (+ non ident.) | Liqs + F + Ap + Gar |
| | 10 | Liqs + F + Ap (+ non ident.) | Liqs + F + Ap + Gar |
| | 24 | Liq + F + Ap | Liqs + F + Ap + Gar |
| | 48 | Liq + F + Ap | Liq + F + Ap + Gar |
| | 100 | Liq + F + Ap | Liq + F + Ap |
| 1300 °C | 1 | Liq + F (+ non ident.) | Liq + F + Ap |
| | 10 | Liq + F + Ap | Liq + F + Ap |
| | 24 | Liq + F + Ap | Liq + F + Ap |
| | 48 | Liq + F + Ap | Liq + F + Ap |
| | 100 | Liq + F + Ap | Liq + F + Ap |
| | (...): small amount | | |

Table 2

Molar ratios of cations in the apatite phases depending on temperatures and periods of interaction. The number of oxygen molecules used per formula was calculated from the formula given below. Aluminium rich apatite (not presented here) differs by an Al_2O_3 ratio of 1–3% rather than by nearly 0% for the main apatite phase from variable substitutions.

| | | 1200 °C | | 1250 °C | | | | 1300 °C | | |
|---|--------------------|---------|---------|---------|---------|---------|---------|---------|---------|---------|
| Annealing temperature | | 1200 °C | 1250 °C | 1300 °C | 1300 °C | 1300 °C |
| Annealing duration | | 100 h | 10 | 24 | 48 | 100 | 10 h | 24 h | 100 h | |
| System | | | | | | | | | | |
| $\text{Gd}_2\text{Zr}_2\text{O}_7$ | CaO | 20,4 | 19,5 | 18,3 | | 18,3 | | | 16,6 | |
| | MgO | 0,0 | 0,0 | 0,0 | | 0,0 | | | 0,0 | |
| | $\text{AlO}_{1,5}$ | 0,2 | 0,3 | 0,1 | | 0,1 | | | 0,2 | |
| | SiO_2 | 37,5 | 38,3 | 37,8 | | 37,5 | | | 38,2 | |
| | $\text{REO}_{1,5}$ | 35,5 | 36,6 | 39,0 | | 39,2 | | | 42,1 | |
| | ZrO_2 | 6,4 | 5,3 | 4,8 | | 5,0 | | | 2,9 | |
| | O per formula | 25,9 | 25,4 | 25,8 | | 26,0 | | | 25,5 | |
| $2\text{ZrO}_2\cdot\text{Y}_2\text{O}_3$ (ss) | CaO | 19,2 | 18,2 | 18,2 | 18,2 | 17,9 | 17,2 | 17,0 | 16,7 | |
| | MgO | 0,4 | 0,3 | 0,4 | 0,4 | 0,3 | 0,5 | 0,4 | 0,3 | |
| | $\text{AlO}_{1,5}$ | 0,3 | 0,3 | 0,4 | 0,2 | 0,2 | 0,4 | 0,2 | 0,1 | |
| | SiO_2 | 37,2 | 37,4 | 37,2 | 37,5 | 37,2 | 37,5 | 37,5 | 37,5 | |
| | $\text{REO}_{1,5}$ | 37,7 | 40,1 | 39,8 | 39,4 | 40,2 | 41,6 | 41,5 | 42,2 | |
| | ZrO_2 | 5,2 | 3,6 | 4,0 | 4,4 | 4,1 | 2,9 | 3,3 | 3,1 | |
| | O per formula | 25,7 | 25,9 | 26,0 | 25,9 | 26,1 | 25,8 | 25,9 | 25,9 | |

However, a higher concentration of structural defects observed in the first phase of interaction is visible for $\text{Gd}_2\text{Zr}_2\text{O}_7$ apatite products (low x_a).

For long interaction periods at 1250 °C, apatite formed from gadolinium zirconate and $2\text{ZrO}_2\cdot\text{Y}_2\text{O}_3$ (ss) is similar with respectively $z_a = 0.9$, $y_a = 0.8$, $x_a = 2 \pm 0.1$ and $z_a = 0.8$, $y_a = 0.6$, $x_a = 2 \pm 0.1$. By contrast, at the beginning of the interaction, the gadolinium apatite structure includes several more defects with a coefficient of $x_a = 1.4$ relative to one of approximately 2 for Y apatite. Gadolinium content levels in the apatite decrease with time while calcium content levels increase as observed by Machnich et al. artificial volcanic ash [56].

3.2.4. Composition of the fluorite phases

For all of the studied temperatures and durations, the formed fluorite is rich in zirconium, RE and calcium. Gd and Y are lost in the pyrochlore and fluorite phases due to RE diffusion in the glass and finally apatite precipitation. Fluorite is obtained through precipitation from dissolved $\text{Gd}_2\text{Zr}_2\text{O}_7$ or $\text{ZrO}_2\cdot\text{Y}_2\text{O}_3$ (ss) in CMAS glass. Ca is dissolved in this fluorite phase.

The composition of the fluorite is only slightly affected by the duration and temperature involved (see Table 3). Only a slight increase in RE content is observed while a concomitant decrease in Ca content in the fluorite is observed as the temperature increases. The nature of rare earth observed is the main parameter, and fluorite formed from

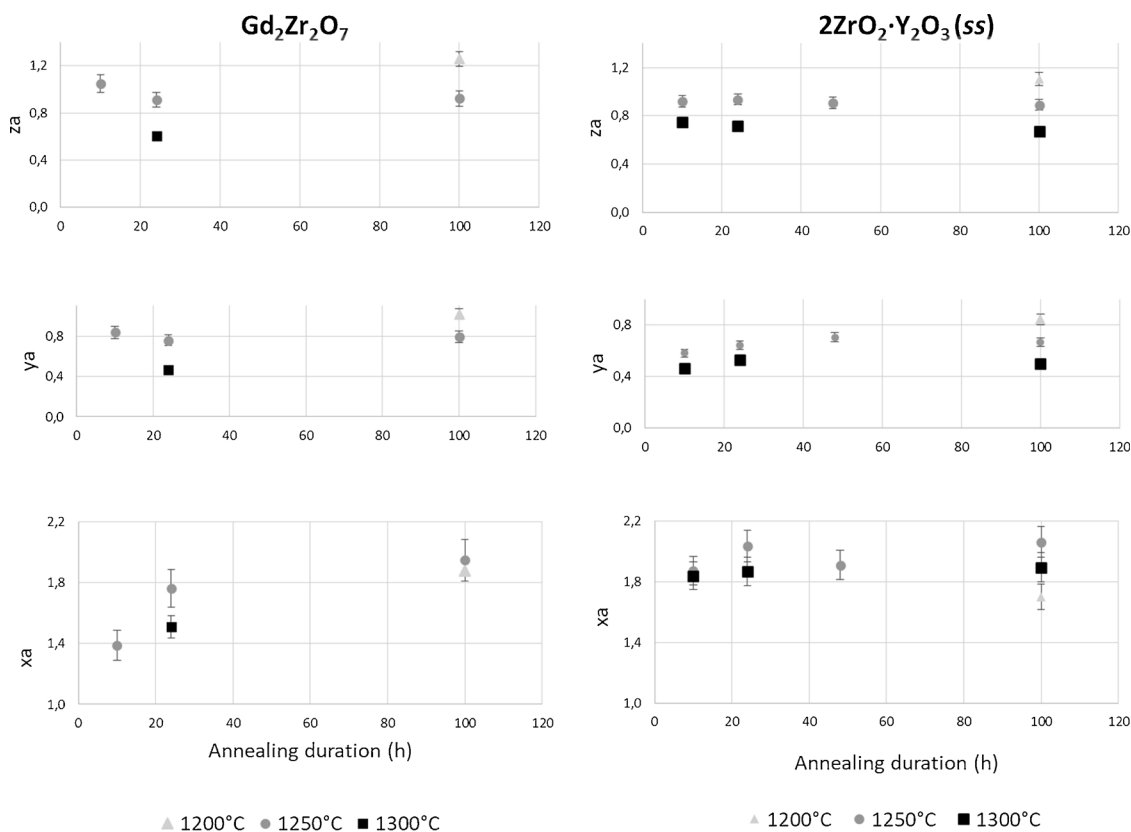


Fig. 8. Number of elements of apatite phases found depending on the annealing period and temperature used in $\text{RE}_{6-y_a}\text{Zr}_{y_a}[\text{RE}_{2-[(2z_a+y_a)/3]}\text{Ca}_{2+z_a}](\text{SiO}_4)_6\text{O}_{x_a}$.

Table 3

Molar ratio of cations in the fluorite phases depending on temperatures and periods of interaction.

| System | T °C | 1200 °C | | 1250 °C | | | 1300 °C | | | |
|---|--------------------|---------|------|---------|------|-------|---------|------|------|-------|
| | Duration | 100 h | 10 h | 24 h | 48 h | 100 h | 10 h | 24 h | 48 h | 100 h |
| Gd ₂ Zr ₂ O ₇ | ZrO ₂ | 80,2 | 79,9 | 78,3 | 80,4 | 79,3 | | 75,9 | | |
| | REO _{1,5} | 12,8 | 12,4 | 15,1 | 12,8 | 13,7 | | 17,3 | | |
| | CaO | 6,1 | 6,2 | 6,1 | 5,7 | 5,8 | | 5,7 | | |
| | SiO ₂ | 0,8 | 1,2 | 0,2 | 0,8 | 0,8 | | 0,8 | | |
| | MgO | 0,0 | 0,0 | 0,2 | 0,2 | 0,2 | | 0,1 | | |
| | AlO _{1,5} | 0,1 | 0,3 | 0,1 | 0,1 | 0,1 | | 0,1 | | |
| 2ZrO ₂ ·Y ₂ O ₃ (ss) | ZrO ₂ | 75,0 | 72,1 | 72,6 | 74,3 | 74,7 | 69,7 | 72,4 | 71,6 | 72,4 |
| | REO _{1,5} | 20,1 | 23,5 | 23,1 | 21,3 | 21,4 | 25,3 | 23,7 | 23,7 | 23,7 |
| | CaO | 3,8 | 3,4 | 3,6 | 3,2 | 3,1 | 3,2 | 3,1 | 3,1 | 3,0 |
| | SiO ₂ | 0,7 | 0,5 | 0,3 | 0,8 | 0,3 | 1,3 | 0,3 | 1,1 | 0,4 |
| | MgO | 0,3 | 0,3 | 0,3 | 0,4 | 0,3 | 0,4 | 0,3 | 0,4 | 0,3 |
| | AlO _{1,5} | 0,1 | 0,2 | 0,2 | 0,1 | 0,1 | 0,2 | 0,2 | 0,2 | 0,1 |

Gd₂Zr₂O₇ consumes more Ca than 2ZrO₂·Y₂O₃ (ss) due to the larger rare earth cation size of gadolinium [26].

3.2.5. Compositions of the garnet phases

Garnet phases A₃²⁺B₃³⁺[SiO₄⁴⁻]₃ with A = Ca, Mg and B=Al, Y with a small amount of Zr are identified from WDS measurements and results of the literature [26,29,57,58]. The garnet phase is a transitional phase detected after CMAS reactions with 2ZrO₂·Y₂O₃ (ss) occur at 1200 °C and 1250 °C. This metastable phase is detected even after 100 h of sintering at 1200 °C and is detected in representative proportions (of more than 7%) for up to 24 h at 1250 °C. This phase mostly contains calcium, yttrium, magnesium, aluminium, silicon and a small amount of zirconium.

It is located mostly found around initial 2ZrO₂·Y₂O₃ (ss) powder and garnet grains present a gradient of composition with higher ratios of yttrium and zirconium in the centre and with higher calcium and silicon ratios found along edges. According to WDS analyses, minimum and maximum gradients in molar percentages of each element (the rest is oxygen) contribute to garnet phase formation: for 10 h at 1250 °C, Y = [2.9–4.9 mol%]; Zr = [1.1–4.8 mol%]; Ca = [9.1–10.9 mol%]; Si = [11.3–14.2 mol%]; Al = [4.9–6.1 mol%]; and Mg = [4.3–5.4 mol%] and for 24 h at 1250 °C, Y = [3.2–7.3 mol%]; Zr = [1.0–1.7 mol%]; Ca = [7.4–10.9 mol%]; Si = [11.7–14.1 mol%]; Al = [5.5–7.9 mol%]; and Mg = [4.5–5.4 mol%].

3.2.6. Residual CMAS composition

As was expected, residual glass is enriched in magnesium and aluminium and is depleted in calcium and silicon (Table 4), which is

Table 4

Molar ratio of cations in the residual glass depending on the temperature and period of interaction.

| System | Annealing temperature | | 1250 °C | | | 1300 °C | | |
|---|-----------------------|-----------|---------|------|-------|---------|------|-------|
| | Annealing duration | CMAS init | 24 h | 48 h | 100 h | 10 h | 24 h | 100 h |
| Gd ₂ Zr ₂ O ₇ | REO _{1,5} | | 1.8 | 1.6 | 1.7 | 1.6 | 1.8 | 1.9 |
| | ZrO ₂ | | 1.4 | 1.5 | 1.5 | 1.7 | 1.4 | 1.6 |
| | CaO | 33 | 30.2 | 29.5 | 30.0 | 30.4 | 30.3 | 29.8 |
| | SiO ₂ | 45 | 40.8 | 43.4 | 42.1 | 44.5 | 40.8 | 42.8 |
| | MgO | 9 | 9.5 | 9.3 | 9.3 | 8.6 | 9.5 | 9.2 |
| | AlO _{1,5} | 13 | 16.3 | 14.7 | 15.4 | 13.1 | 16.3 | 14.7 |
| 2ZrO ₂ ·Y ₂ O ₃ (ss) | Si:Ca ratio | | 1.4 | 1.5 | 1.4 | 1.5 | 1.3 | 1.4 |
| | REO _{1,5} | | 2.3 | 2.3 | 3.9 | 2.6 | 2.3 | 2.8 |
| | ZrO ₂ | | 1.2 | 1.2 | 1.4 | 1.1 | 1.1 | 1.2 |
| | CaO | 33 | 29.6 | 30.6 | 30.7 | 30.9 | 30.6 | 30.6 |
| | SiO ₂ | 45 | 43.3 | 40.8 | 41.1 | 40.6 | 41.5 | 41.5 |
| | MgO | 9 | 9.2 | 9.4 | 9.9 | 9.6 | 9.3 | 9.3 |
| | AlO _{1,5} | 13 | 14.2 | 13.8 | 14.6 | 15.5 | 14.6 | 14.6 |
| | Si:Ca ratio | | 1.5 | 1.3 | 1.3 | 1.3 | 1.3 | 1.4 |

coherent with depletion observed in calcium and silicon correlated with the formation of Ca, Si-rich apatite phase and Ca-rich fluorite phases.

Yttrium, gadolinium and zirconium are found in small proportions in the glass (1 to 2%) except for yttrium observed after 100 h at 1250 °C, which is found at 4%. This rather surprising value may be related to the transformation of the garnet phase and must correspond to partial or complete dissolution in the glass. The solubility limit of yttrium for residual CMAS is higher than that of gadolinium (2.3–3.9% vs. 1.6–1.9%). This is in accordance with the literature, and Poerschke specifically found a value of roughly 3.2 mol% for Y solubility (Y from Y₄Zr₃O₁₂) in C₃₃M₉A₁₃S₄₅ and a value of 2.5 mol% for Gd (from Gd₂Zr₂O₇).

4. Discussion

4.1. Morphology of the interaction zone

Spherical product agglomerates form from rapid reactions occurring between CMAS and spherical raw material Gd₂Zr₂O₇ while reaction products spread across the remaining CMAS for 2ZrO₂·Y₂O₃ (ss). In the literature, slower formation speeds of apatite for Y-based apatite than for Gd-based apatite have been demonstrated [43]. This is also a consequence of the higher solubility of Y relative to that of Gd in the glass, leading to Gd-apatite crystallization with lower rare earth concentrations in the glass. This study shows that differences in reaction speeds are at stake in the very first stages (< 1 h) of CMAS interactions occurring between Gd zirconate and 2ZrO₂·Y₂O₃ (ss).

Such behaviour is similar to that explaining morphologies of

interaction zones in the pellets. Indeed, for gadolinium zirconate products form a continuous layer while a non-continuous product zone is obtained with slower reacting $2\text{ZrO}_2\cdot\text{Y}_2\text{O}_3$ (ss).

Then, a simple powder/powder study is representative of real behaviours of the anti-CMAS system. This can be generalized by examining phenomena involving agglomerated anti-CMAS particles over short enough periods to observe the morphology of products formed around dissolving particles.

4.2. Residual glass properties

The composition of residual molten CMAS is modified during the formation of reaction products: by the dissolution-precipitation of RE^{3+} and Zr^{4+} and through the formation of an apatite phase rich in RE^{3+} , Ca^{2+} , Si^{4+} , and Zr^{4+} and of a fluorite phase with Zr^{4+} , RE^{3+} and with a small amount of Ca^{2+} . This results in the depletion of Ca^{2+} and Si^{4+} cations in the silicate glass. This results in the local supersaturation of magnesium Mg^{2+} and aluminium Al^{3+} cations within the glass.

The viscosity of residual glass observed after long interaction periods (100 h interactions observed at 1250 °C and 1300 °C) was calculated from the GRD model [58]. Under these conditions, SiO_2 concentrations reached 42–43 mol % while Si:Ca ratios reached 1.3 – 1.5. According to calculations, viscosity values of the residual glass ($\sim 10^{-2}$ Pa.s) are one range of order lower than those of the initial $\text{C}_{33}\text{M}_9\text{A}_{13}\text{S}_{45}$ ($\sim 10^{-1}$ Pa.s). Then, the viscosity of the residual glass decreases by one order of magnitude after CMAS interactions with anti-CMAS powders occur. This is expected to largely influence rates of CMAS infiltration observed in porous anti-CMAS materials.

4.3. Metastable phases

The progressive dissolution of rare earth RE^{3+} (RE = Gd or Y) and zirconium Zr^{4+} cations from $\text{Gd}_2\text{Zr}_2\text{O}_7$ and $2\text{ZrO}_2\cdot\text{Y}_2\text{O}_3$ (ss) anti-CMAS materials occurs in molten CMAS. As the concentration of RE and Zr ions reaches a critical threshold, disordered fluorite and apatite phase can crystallize from the glass. These two phases are the only phases observed at equilibrium. By contrast, under non-stationary conditions, transition phases are observed. They are found across a larger range of temperatures and periods in a yttrium-based system. These phases can help prevent CMAS infiltration for rapid formation and high temperatures. However, according to the literature garnet phase exhibits slower formation kinetics than Gd apatite [59]. Then, the formation of garnet is not expected to favour CMAS tightness.

Unlike the apatite phase, the garnet phase traps magnesium and aluminium cations from molten CMAS such that reactions necessary to form the garnet phase lead to a less significant decrease in viscosity than that of one order of magnitude observed under steady state conditions. However, within the framework of this study the exact composition of the residual glass could not be measured.

4.4. Role of zirconium cations

Gadolinium zirconate $\text{Gd}_2\text{Zr}_2\text{O}_7$ and $2\text{ZrO}_2\cdot\text{Y}_2\text{O}_3$ (ss) form two reaction products containing zirconium: Zr substituted apatite phase and disordered fluorite phase. The involvement of zirconium in the formation of reaction products for anti-CMAS effects remains unknown. It is deleterious in decreasing the proportion of calcium trapped in apatite relative to zirconium free systems, but it is favourable in forming solid reaction products with lower CMAS proportions.

4.5. Evolution of apatite phase compositions

The apatite phase formula is written as $\text{RE}_{6-ya}\text{Zr}_{ya}[\text{RE}_{2-(2za+ya)}]_{33}\text{Ca}_{2+za}(\text{SiO}_4)_6\text{O}_{xa}$ for both yttrium and gadolinium systems. At a steady state, coefficients x, y and z are similar for yttrium and

gadolinium systems (cf. paragraph 3.2.3). Equilibrium compositions are valued at $\text{Gd}_{6.7}\text{Zr}_{0.6}\text{Ca}_{2.8}(\text{SiO}_4)_6\text{O}_2$ and $\text{Y}_{6.3}\text{Zr}_{0.8}\text{Ca}_{2.9}(\text{SiO}_4)_6\text{O}_2$. Yttrium apatite requires slightly less rare earth to form than gadolinium-based systems. While this may facilitate anti-CMAS behaviour, the rest of this study shows that it cannot compensate for the difference in reaction kinetics observed between the two systems.

A major difference is detected over short interaction periods: for the yttrium-based system the apatite formula is the same as the equilibrium formula (with 10 h of interaction) while for the gadolinium system apatite formed in the transient state presents more defects ($x = 1.4$). The system reaches equilibrium after several tens of hours with an x value of 2.

Then, for gadolinium-based zirconates, defect-rich apatite first forms, which correlates with strong kinetics of product formation observed for this system relative to those of yttrium systems.

4.6. Implications for the development of anti-CMAS materials

Rapid kinetics of reaction product formation are needed for anti-CMAS products to be sufficiently CMAS tight during initial infiltration. Then, the nature of the phase observed at equilibrium may not be sufficiently indicative of the efficiency of the system. Kinetics relative to the RE solubility of glass and to apatite phase formation favour gadolinium as noted by other authors [26].

To develop more insight into the capacities of anti-CMAS material, CMAS / anti-CMAS interactions must be observed over very short interaction periods. In situ methods are very difficult and costly to apply under high temperatures. This paper shows that with basic SEM observations capacities of the anti-CMAS system can be assessed from observations of the morphologies of interaction zones positioned around agglomerated raw materials. Such research can provide information that can facilitate the development of anti-CMAS systems.

5. Conclusion

A simple experimental setup for the examination of kinetics of the high temperature potential of anti-CMAS systems was developed. It was efficient to determine the composition and morphology of reaction products observed during initial interaction phases of CMAS / anti-CMAS interaction (1 h or less) and to compare them to steady state conditions.

Under steady state conditions, $2\text{ZrO}_2\cdot\text{Y}_2\text{O}_3$ (ss) traps slightly more calcium in formed apatite (1 Ca^{2+} for 2.2 Y^{3+}) than gadolinium zirconate $\text{Gd}_2\text{Zr}_2\text{O}_7$ (1 Ca^{2+} for 2.4 Gd^{3+}). However, stronger effects of apatite formation kinetics than apatite compositions on anti-CMAS behaviour are found in this study.

Gadolinium zirconate interactions with CMAS benefit from the low solubility of gadolinium ions found in CMAS glass and from high rates of apatite reaction kinetics. This results in the formation of large quantities of reaction products from the start of interactions within the vicinity of raw material $\text{Gd}_2\text{Zr}_2\text{O}_7$. This also leads to the development of a continuous layer of reaction products in $\text{Gd}_2\text{Zr}_2\text{O}_7$ pellets at the interface between non-reacted gadolinium zirconate pellets and CMAS.

For gadolinium zirconate, apatite with a higher ratio of rare earth forms at the start of the interaction. However, the higher consumption of rare earth for the formation of reaction products does not hinder anti-CMAS performance due to rapid kinetics of apatite formation and low levels of gadolinium solubility found in CMAS. This may even be more favourable, as it results in a lower consumption of Ca and Si in glass and then to a lesser decline in the viscosity of residual CMAS. For both gadolinium zirconate and $2\text{ZrO}_2\cdot\text{Y}_2\text{O}_3$ (ss) systems, the composition of respective fluorite does not evolve with time or temperature. The lower kinetics of $2\text{ZrO}_2\cdot\text{Y}_2\text{O}_3$ (ss) systems are also illustrated by the larger range of temperatures and periods over which large amounts of metastable phases are found. While these phases are rich in CMAS elements, their formation kinetics are slower than those of gadolinium

apatite and fluorite products, which may explain why garnet formation does not effectively prevent CMAS infiltration.

Differences in transient and steady states of the two studied anti-CMAS systems demonstrate the importance of studying anti-CMAS/CMAS interactions occurring under transient conditions. This is exemplified for gadolinium zirconate and $2\text{ZrO}_2\text{-Y}_2\text{O}_3$ (ss) with similar compositions and quantities of reaction products at equilibrium while anti-CMAS behaviours observed under real conditions are better understood thanks to considerable variations in transient states detected.

In addition to evaluating these specific systems, this study proposes a simple experimental approach to the comparative study of anti-CMAS systems. The study of agglomerated powders interacting with CMAS allows one to observe transient states and to evaluate the capacity for anti-CMAS material to prevent CMAS infiltration in real systems. From the proposed approach we discriminate two interpretations of CMAS infiltration on pellets: when a small number of reaction products is present, it occurs due to low kinetics of product formation or from the desired CMAS tightness of reaction products.

Acknowledgements

This work was supported by the French Defence Research Organization (DGA) and by the SAFRAN Group.

We would like to thank the Raimond Castaing Microanalysis Centre and specifically S. Gouy and S. Le Blond du Plouy for their assistance with EPMA analyses and SEM-FEG microscopy tasks.

References

- [1] U. Schulz, C. Leyens, K. Fritscher, M. Peters, B. Saruhan-Brings, O. Lavigne, J.M. Dorvaux, M. Poulain, R. Mevrel, M. Caliez, Some recent trends in research and technology of advanced thermal barrier coatings, *Aerosp. Sci. Technol.* 7 (2003) 73–80, [https://doi.org/10.1016/S1270-9638\(02\)00003-2](https://doi.org/10.1016/S1270-9638(02)00003-2).
- [2] M. Peters, C. Leyens, U. Schulz, W.A. Kaysser, EB-PVD thermal barrier coatings for aeroengines and gas turbines, *Adv. Eng. Mater.* 3 (4) (2001) 193–204, [https://doi.org/10.1002/1527-2648\(200104\)3:4<193::AID-ADEM193>3.0.CO;2-U](https://doi.org/10.1002/1527-2648(200104)3:4<193::AID-ADEM193>3.0.CO;2-U).
- [3] D.J. De Wet, R. Taylor, F.H. Stott, Corrosion mechanisms of $\text{ZrO}_2\text{-Y}_2\text{O}_3$ thermal barrier coatings in the presence of molten middle-east sand, *J. Phys. IV 3* (C9) (1993) C9–655, <https://doi.org/10.1051/jp4:1993969>.
- [4] F.H. Stott, D.J. de Wet, R. Taylor, Degradation of thermal-barrier coatings at very high temperatures, *MRS Bull.* 19 (10) (1994) 46–49, <https://doi.org/10.1557/S0883769400048223>.
- [5] M.P. Borom, C.A. Johnson, L.A. Peluso, Role of environment deposits and operating surface temperature in spallation of air plasma sprayed thermal barrier coatings, *Surf. Coat. Technol.* 86 (1996) 116–126, [https://doi.org/10.1016/S0257-8972\(96\)02994-5](https://doi.org/10.1016/S0257-8972(96)02994-5).
- [6] A. Aygun, A.L. Vasiliev, N.P. Padture, X. Ma, Novel thermal barrier coatings that are resistant to high-temperature attack by glassy deposits, *Acta Mater.* 55 (20) (2007) 6734–6745, <https://doi.org/10.1016/j.actamat.2007.08.028>.
- [7] W. Braue, Environmental stability of the YSZ layer and the YSZ/TGO interface of an in-service EB-PVD coated high-pressure turbine blade, *J. Mater. Sci.* 44 (7) (2009) 1664–1675, <https://doi.org/10.1007/s10853-008-3215-8>.
- [8] M.H. Vidal-Sétif, C. Rio, D. Boivin, O. Lavigne, Microstructural characterization of the interaction between 8YPSZ (EB-PVD) thermal barrier coatings and a synthetic CAS, *Surf. Coat. Technol.* 239 (2014) 41–48, <https://doi.org/10.1016/j.surfcoat.2013.11.014>.
- [9] M.H. Vidal-Sétif, N. Chellah, C. Rio, C. Sanchez, O. Lavigne, Calcium-magnesium-alumino-silicate (CMAS) degradation of EB-PVD thermal barrier coatings: characterization of CMAS damage on ex-service high pressure blade TBCs, *Surf. Coat. Technol.* 208 (2012) 39–45, <https://doi.org/10.1016/j.surfcoat.2012.07.074>.
- [10] S. Krämer, J. Yang, C.G. Levi, C.A. Johnson, Thermochemical interaction of thermal barrier coatings with molten $\text{CaO-MgO-Al}_2\text{O}_3\text{-SiO}_2$ (CMAS) deposits, *J. Am. Ceram. Soc.* 89 (10) (2006) 3167–3175, <https://doi.org/10.1111/j.1551-2916.2006.01209.x>.
- [11] S. Krämer, et al., Mechanisms of cracking and delamination within thick thermal barrier systems in aero-engines subject to calcium-magnesium-alumino-silicate (CMAS) penetration, *Mater. Sci. Eng. A* 490 (1–2) (2008) 26–35, <https://doi.org/10.1016/j.msea.2008.01.006>.
- [12] C. Mercer, S. Faulhaber, A.G. Evans, R. Darolia, A delamination mechanism for thermal barrier coatings subject to calcium-magnesium-alumino-silicate (CMAS) infiltration, *Acta Mater.* 53 (4) (2005) 1029–1039, <https://doi.org/10.1016/j.actamat.2004.11.028>.
- [13] U. Schulz, W. Braue, Degradation of $\text{La}_2\text{Zr}_2\text{O}_7$ and other novel EB-PVD thermal barrier coatings by CMAS ($\text{CaO-MgO-Al}_2\text{O}_3\text{-SiO}_2$) and volcanic ash deposits, *Surf. Coat. Technol.* 235 (2013) 165–173, <https://doi.org/10.1016/j.surfcoat.2013.07.029>.
- [14] S.R. Gislason, et al., Characterization of Eyjafjallajökull volcanic ash particles and a protocol for rapid risk assessment, *Proc. Natl. Acad. Sci.* 108 (18) (2011) 7307–7312, <https://doi.org/10.1073/pnas.1015053108>.
- [15] P. Rossini, et al., April-May 2010 Eyjafjallajökull volcanic fallout over Rimini, Italy, *Atmos. Environ.* 48 (2012) 122–128, <https://doi.org/10.1016/j.atmosenv.2011.05.018>.
- [16] B. Langmann, A. Folch, M. Hensch, V. Matthias, Volcanic ash over Europe during the eruption of Eyjafjallajökull on Iceland, April-May 2010, *Atmos. Environ.* 48 (2012) 1–8, <https://doi.org/10.1016/j.atmosenv.2011.03.054>.
- [17] N. Chellah, Contribution à la compréhension de la dégradation chimique de barrière thermique en zircone yttrée par les CMAS en vue de proposer une nouvelle composition céramique résistante dans le système $\text{ZrO}_2\text{-Nd}_2\text{O}_3$, Ph.D. manuscript, Université de Lorraine, ONERA, 2013.
- [18] G. Pujol, F. Ansart, J.-P. Bonino, A. Malié, S. Hamadi, Step-by-step investigation of degradation mechanisms induced by CMAS attack on YSZ materials for TBC applications, *Surf. Coat. Technol.* 237 (2013) 71–78, <https://doi.org/10.1016/j.surfcoat.2013.08.055>.
- [19] F. Perrudin, C. Rio, M.H. Vidal-Sétif, C. Petitjean, P.J. Panteix, M. Vilasi, Gadolinium oxide solubility in molten silicate: dissolution mechanism and stability of $\text{Ca}_2\text{Gd}_3(\text{SiO}_4)_6\text{O}_2$ and $\text{Ca}_3\text{Gd}_2(\text{Si}_3\text{O}_9)_2$ silicate phases, *J. Eur. Ceram. Soc.* 37 (7) (2017) 2657–2665, <https://doi.org/10.1016/j.jeurceramsoc.2017.02.022>.
- [20] R. Vassen, X. Cao, F. Tietz, D. Basu, D. Stöver, Zirconates as new materials for thermal barrier coatings, *J. Am. Ceram. Soc.* 83 (8) (2000) 2023–2028, <https://doi.org/10.1111/j.1151-2916.2000.tb01506.x>.
- [21] A.R. Krause, et al., $2\text{ZrO}_2\text{-Y}_2\text{O}_3$ thermal barrier coatings resistant to degradation by molten CMAS: part I, optical basicity considerations and processing, *J. Am. Ceram. Soc.* 97 (12) (2014) 3943–3949, <https://doi.org/10.1111/jace.13210>.
- [22] J. Wu, et al., Low-thermal-conductivity rare-earth zirconates for potential thermal-barrier-coating applications, *J. Am. Ceram. Soc.* 85 (12) (2002) 3031–3035, <https://doi.org/10.1111/j.1151-2916.2002.tb00574.x>.
- [23] M. Kumar, I.A. Raj, R. Pattabiraman, $2\text{ZrO}_2\text{-Y}_2\text{O}_3$ (ss). (YZ)-pyrochlore based oxide as an electrolyte material for intermediate temperature solid oxide fuel cells (ITSOFCs)—Influence of Mn addition on YZ, *Mater. Chem. Phys.* 108 (1) (2008) 102–108, <https://doi.org/10.1016/j.matchemphys.2007.09.010>.
- [24] F. Fu-K'ang, A.K. Kuznetsov, É. Keler, Phase relationships in the $\text{Y}_2\text{O}_3\text{-ZrO}_2$ system, *Russ. Chem. Bull.* 11 (7) (1962) 1071–1075, <https://doi.org/10.1007/BF00908375>.
- [25] D.R. Clarke, S.R. Phillpot, Thermal barrier coating materials, *Mater. Today* 8 (6) (2005) 22–29, [https://doi.org/10.1016/S1369-7021\(05\)70934-2](https://doi.org/10.1016/S1369-7021(05)70934-2).
- [26] D.L. Poerschke, T.L. Barth, C.G. Levi, Equilibrium relationships between thermal barrier oxides and silicate melts, *Acta Mater.* 120 (2016) 302–314, <https://doi.org/10.1016/j.actamat.2016.08.077>.
- [27] A.R. Krause, H.F. Garces, B.S. Senturk, N.P. Padture, $2\text{ZrO}_2\text{-Y}_2\text{O}_3$ thermal barrier coatings resistant to degradation by molten CMAS: part II, interactions with sand and fly ash, *J. Am. Ceram. Soc.* 97 (12) (2014) 3950–3957, <https://doi.org/10.1111/jace.13209>.
- [28] K.M. Grant, S. Kramer, G.G.E. Seward, C.G. Levi, Calcium-magnesium alumino-silicate interaction with yttrium monosilicate environmental barrier coatings: YMS interaction with YMS EBCs, *J. Am. Ceram. Soc.* 93 (10) (2010) 3504–3511, <https://doi.org/10.1111/j.1551-2916.2010.03916.x>.
- [29] N.K. Eils, P. Mechnich, W. Braue, Effect of CMAS deposits on MOCVD coatings in the system $\text{Y}_2\text{O}_3\text{-ZrO}_2$: phase relationships, *J. Am. Ceram. Soc.* 96 (10) (2013) 3333–3340, <https://doi.org/10.1111/jace.12502>.
- [30] W. Li, H. Zhao, X. Zhong, L. Wang, S. Tao, Air plasma-sprayed yttria and yttria-stabilized zirconia thermal barrier coatings subjected to calcium-magnesium-alumino-silicate (CMAS), *J. Therm. Spray Technol.* 23 (6) (2014) 975–983, <https://doi.org/10.1007/s11666-014-0107-0>.
- [31] D.L. Poerschke, T.L. Barth, O. Fabricznaya, C.G. Levi, Phase equilibria and crystal chemistry in the calcia-silica-yttria system, *J. Eur. Ceram. Soc.* 36 (7) (2016) 1743–1754, <https://doi.org/10.1016/j.jeurceramsoc.2016.01.046>.
- [32] H. Wang, Reaction Mechanism of $\text{CaO-MgO-Al}_2\text{O}_3\text{-SiO}_2$ (CMAS) on Lanthanide Zirconia Thermal Barrier Coatings, Ph.D manuscript, Auburn University, Alabama, 2016, p. 151.
- [33] H. Wang, A. Bakal, X. Zhang, E. Tarwater, Z. Sheng, J.W. Fergus, $\text{CaO-MgO-Al}_2\text{O}_3\text{-SiO}_2$ (CMAS) corrosion of $\text{Gd}_2\text{Zr}_2\text{O}_7$ and $\text{Sm}_2\text{Zr}_2\text{O}_7$, *J. Electrochem. Soc.* 163 (10) (2016) C643–C648, <https://doi.org/10.1149/2.0301610jes>.
- [34] D.L. Poerschke, C.G. Levi, Phase equilibria in the calcia-gadolinia-silica system, *J. Alloys Compd.* 695 (2017) 1397–1404, <https://doi.org/10.1016/j.jallcom.2016.10.263>.
- [35] S. Krämer, J. Yang, C.G. Levi, Infiltration-inhibiting reaction of gadolinium zirconate thermal barrier coatings with CMAS melts, *J. Am. Ceram. Soc.* 91 (2) (2008) 576–583, <https://doi.org/10.1111/j.1551-2916.2007.02175.x>.
- [36] J.M. Drexler, Thermal Barrier Coatings Resistant to Glassy Deposits, Ph.D. manuscript The Ohio State University, 2011.
- [37] J.M. Drexler, A.L. Ortiz, N.P. Padture, Composition effects of thermal barrier coating ceramics on their interaction with molten Ca-Mg-Al-silicate (CMAS) glass, *Acta Mater.* 60 (15) (2012) 5437–5447, <https://doi.org/10.1016/j.actamat.2012.06.053>.
- [38] K.M. Doleker, A.C. Karaoglanli, Comparison of oxidation behavior of YSZ and $\text{Gd}_2\text{Zr}_2\text{O}_7$ thermal barrier coatings (TBCs), *Surf. Coat. Technol.* 318 (2017) 198–207, <https://doi.org/10.1016/j.surfcoat.2016.12.078>.
- [39] E.M. Zaleski, C.A. Ensslen, C.G. Levi, Mechanism and Mitigation of CMAS attack on

- Thermal Barrier Coatings, Ph.D. manuscript University of California, Santa Barbara, 2013.
- [40] M.H. Habibi, L. Wang, S.M. Guo, Evolution of hot corrosion resistance of YSZ, $Gd_2Zr_2O_7$, and $Gd_2Zr_2O_7$ +YSZ composite thermal barrier coatings in Na_2SO_4 +V2O5 at 1050°C, *J. Eur. Ceram. Soc.* 32 (8) (2012) 1635–1642, <https://doi.org/10.1016/j.jeurceramsoc.2012.01.006>.
- [41] W. Deng, J.W. Fergus, Effect of CMAS composition on hot corrosion behavior of gadolinium zirconate thermal barrier coating materials, *J. Electrochem. Soc.* 164 (9) (2017) C526–C531, <https://doi.org/10.1149/2.0531709jes>.
- [42] G. Moskal, et al., Characterization of microstructure and thermal properties of $Gd_2Zr_2O_7$ -type thermal barrier coating, *J. Eur. Ceram. Soc.* 32 (9) (2012) 2025–2034, <https://doi.org/10.1016/j.jeurceramsoc.2011.11.043>.
- [43] A. Quintas, D. Caurant, O. Majéris, J.L. Dussossoy, T. Charpentier, Effect of changing the rare earth cation type on the structure and crystallization behavior of an aluminoborosilicate glass, *Phys. Chem. Glasses – Eur. J. Glass Sci. Technol. Part B* 49 (4) (2008) 192–197.
- [44] E.M. Zaleski, C. Ensslen, C.G. Levi, Melting and crystallization of silicate systems relevant to thermal barrier coating damage, *J. Am. Ceram. Soc.* 98 (5) (2015) 1642–1649, <https://doi.org/10.1111/jace.13478>.
- [45] A.R. Krause, X. Li, N.P. Padture, Interaction between ceramic powder and molten calcia-magnesia-alumino-silicate (CMAS) glass, and its implication on CMAS-resistant thermal barrier coatings, *Scr. Mater.* 112 (2016) 118–122, <https://doi.org/10.1016/j.scriptamat.2015.09.027>.
- [46] R. Wellman, G. Whitman, J.R. Nicholls, CMAS corrosion of EB PVD TBCs: identifying the minimum level to initiate damage, *Int. J. Refract. Met. Hard Mater* 28 (1) (2010) 124–132, <https://doi.org/10.1016/j.ijrmhm.2009.07.005>.
- [47] P. Mohan, Environmental Degradation of Oxidation Resistant and Thermal Barrier Coatings for Fuel-Flexible Gas Turbine Applications, Ph.D. manuscript University of Central Florida, 2010.
- [48] G. Pujol, Elaboration par voie sol-gel de nouvelles barrières thermiques architecturées présentant des propriétés contre l'infiltration des oxydes CMAS (Ca, Mg, Al, Si) - Etude de la réparabilité de systèmes endommagés, Ph.D. manuscript Université Toulouse III Paul Sabatier, 2014.
- [49] J.L. Pouchou, F. Pichoir, *Recherche Aérospatiale* 3 (1984) 167–192.
- [50] B.E. Scheetz, W.B. White, Characterization of anion disorder in zirconate $A_2B_2O_7$ compounds by Raman spectroscopy, *J. Am. Ceram. Soc.* 62 (9–10) (1979) 468–470, <https://doi.org/10.1111/j.1151-2916.1979.tb19107.x>.
- [51] P.E.R. Blanchard, et al., Does local disorder occur in the pyrochlore zirconates? *Inorg. Chem.* 51 (24) (2012) 13237–13244, <https://doi.org/10.1021/ic301677b>.
- [52] B.P. Mandal, P.S.R. Krishna, A.K. Tyagi, Order-disorder transition in the $Nd_{2-y}Y_zZr_2O_7$ system: probed by X-ray diffraction and Raman spectroscopy, *J. Solid State Chem.* 183 (1) (2010) 41–45, <https://doi.org/10.1016/j.jssc.2009.10.010>.
- [53] B.P. Mandal, A. Banerji, V. Sathe, S.K. Deb, A.K. Tyagi, Order-disorder transition in $Nd_{2-y}Gd_yZr_2O_7$ pyrochlore solid solution: an X-ray diffraction and Raman spectroscopic study, *J. Solid State Chem.* 180 (10) (2007) 2643–2648, <https://doi.org/10.1016/j.jssc.2007.07.007>.
- [54] Y.H. Lee, H.S. Sheu, J.P. Deng, H.-C.I. Kao, Preparation and fluorite-pyrochlore phase transformation in $Gd_2Zr_2O_7$, *J. Alloys Compd.* 487 (1–2) (2009) 595–598, <https://doi.org/10.1016/j.jallcom.2009.08.021>.
- [55] H.Y. Xiao, F. Gao, W.J. Weber, Ab initio investigation of phase stability of $Y_2Ti_2O_7$ and $Y_2Zr_2O_7$ under high pressure, *Phys. Rev. B* 80 (21) (2009), <https://doi.org/10.1103/PhysRevB.80.212102>.
- [56] P. Mechnich, W. Braue, Volcanic ash-induced decomposition of EB-PVD $Gd_2Zr_2O_7$ thermal barrier coatings to Gd-oxypatite, zircon, and Gd, Fe-zirconolite, *J. Am. Ceram. Soc.* 96 (1958) 2013, <https://doi.org/10.1111/jace.12251>.
- [57] D.L. Poerschke, C.G. Levi, Effects of cation substitution and temperature on the interaction between thermal barrier oxides and molten CMAS, *J. Eur. Ceram. Soc.* 35 (2) (2015) 681–691, <https://doi.org/10.1016/j.jeurceramsoc.2014.09.006>.
- [58] D.L. Poerschke, D.D. Hass, S. Eustis, G.G.E. Seward, J.S. Van Sluytman, C.G. Levi, Stability and CMAS resistance of ytterbium-silicate/hafnate EBCs/TBC for SiC composites, *J. Am. Ceram. Soc.* 98 (1) (2015) 278–286, <https://doi.org/10.1111/jace.13262>.
- [59] C.G. Levi, J.W. Hutchinson, M.-H. Vidal-Sétif, C.A. Johnson, Environmental degradation of thermal-barrier coatings by molten deposits, *MRS Bull.* 37 (10) (2012) 932–941, <https://doi.org/10.1557/mrs.2012.230>.